ACS APPLIED MATERIALS & INTERFACES

Research Article

www.acsami.org

One-Step Synthesis of Si@C Nanoparticles by Laser Pyrolysis: High-Capacity Anode Material for Lithium-Ion Batteries

Julien Sourice,*[,†,‡,§] Axelle Quinsac,[†] Yann Leconte,[†] Olivier Sublemontier,[†] Willy Porcher,[‡,§] Cedric Haon,[‡,§] Arnaud Bordes,[‡,⊥] Eric De Vito,[‡,⊥] Adrien Boulineau,[‡,§] Séverine Jouanneau Si Larbi,[‡,§] Nathalie Herlin-Boime,*[,†] and Cécile Reynaud[†]

[†]CNRS UMR 3685, NIMBE, IRAMIS, CEA, F-91191 Gif sur Yvette, France

[‡]Université Grenoble Alpes, F-38000, Grenoble, France

[§]LITEN and [⊥]MINATEC, CEA, 17 rue des Martyrs, F-38054 Grenoble, France

Supporting Information

ABSTRACT: Carbon-covered silicon nanoparticles (Si@C) were synthesized for the first time by a one-step continuous process in a novel two stages laser pyrolysis reactor. Crystallized silicon cores formed in a first stage were covered in the second stage by a continuous shell mainly consisting in low organized sp^2 carbon. At the Si/C interface silicon carbide is absent. Moreover, the presence of silicon oxide is reduced compared to materials synthesized in several steps, allowing the use of such material as promising anode material in lithium-ion batteries (LIB). Auger Electron Spectroscopy (AES) analysis of the samples at both Si_{KLL} and Si_{LVV} edges proved the uniformity of the carbon coating. Cyclic voltammetry was used to compare the stability of Si and Si@C active materials. In half-cell configuration, Si@C exhibits a high and stable capacity of 2400 mAh g^{-1} at C/10 and up to 500 mAh g^{-1} over 500 cycles at 2C. The retention of the capacity is attributed to the protective effect of the carbon shell, which avoids direct contact between the silicon surface and the electrolyte.

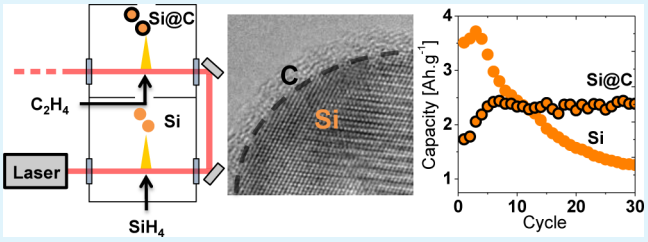

KEYWORDS: *laser pyrolysis, core−shell nanoparticle, silicon, carbon, lithium-ion battery*

INTRODUCTION

Li-ion battery (LIB) is one of the most popular energy storage systems in consumer electronic and electric vehicle applications. The anode of such devices is based on graphite, which shows great cyclability but low specific capacity. In this context, silicon appears as an abundant and relevant candidate for graphite replacement.[1−4] Its high theoretical specific capacity (3579 mAh g^{-1} for the lithiated phase $Li_{3,75}Si$) can multiply by ten the amount of lithium stored in the anode as compared to the common graphite one (372 mAh g^{-1}). Furthermore, the low discharge potential of Si, about 0.4 V against Li/Li^+ redox couple can provide high specific energy to this technology.[5] However, direct substitution of carbon by micrometer-sized silicon particles often leads to a very limited stability, usually less than 100 cycles. The huge volume expansion of silicon alloys upon lithiation results in electrical contact loss and pulverization of the material. Moreover, the solid electrolyte interphase (SEI), because of the decomposition of the electrolyte below 1 V vs Li/Li^+ at the silicon surface, is continuously damaged by the volume expansion of silicon. The combination of these two effects leads to the filling of the electrode porosity by SEI and rapid fading of the capacity.[6−8]

Having in mind to overcome these drawbacks and stabilize Si-based anode, various solutions have been explored. Different components like binders, conducting percolators or electrochemically polymerizable carbonate compounds, were added to the anode formulation and the electrolyte in order to extend the cycling stability.[9−12] In a complementary approach, varying the size or the morphology of silicon was actively studied. For example, Y. Cui et al. reported a double-walled silicon nanotube based anode ables to withstand 6000 stable cycles at 12C.[13] Decreasing the size of silicon particles in the nanometer domain also allowed drastic stability improvements.[14] Moreover, covering the silicon active material with a protective layer has been considered by many studies.[15−18] It can isolates silicon from direct exposure to electrolyte thus greatly limiting the formation of thick SEI layer. The formation of a carbon shell around silicon nanoparticles is one of the most cited method ensuring an effective protection and both acting as ionic and electronic conductor.[19,20] Its preparation is usually performed through thermal decomposition of a carbonaceous polymeric precursor on the surface of silicon particles.[21,22] However, such multisteps and batch to batch processes involve manipulation of nanopowders as well as air exposure and oxidation of the silicon surface. Nonthermic plasma synthesis reported by Agarwal et al. is an interesting way to obtain silicon carbon core−shell

Received: December 23, 2014
Accepted: March 11, 2015
Published: March 11, 2015

ACS Publications © 2015 American Chemical Society

DOI: 10.1021/am5089742
ACS Appl. Mater. Interfaces 2015, 7, 6637−6644

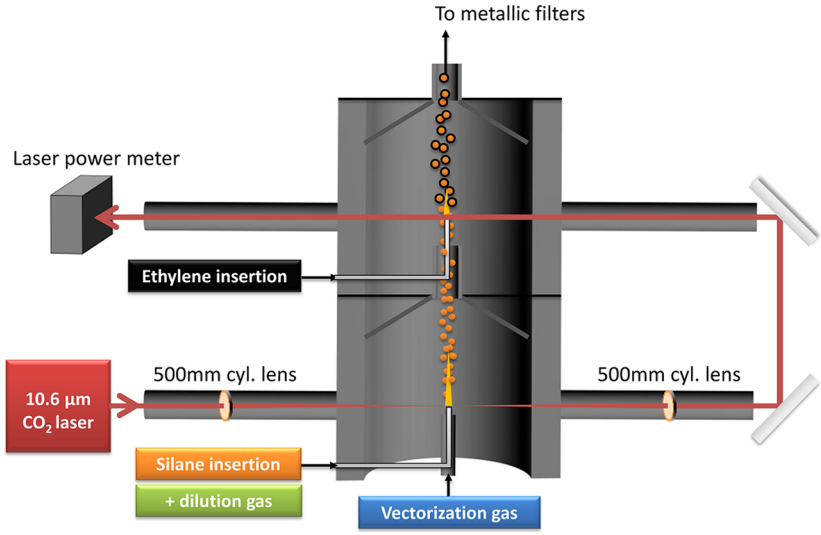

Figure 1. Schematic diagram of the laser pyrolysis reactor in the two stages configuration.

nanoparticles in a single step.[23] However, the small quantity of final product and the presence of silicon carbide at the core−shell interface prevents its use as anode material.

In the present paper, we report a new single-step process to synthesize large quantity of core−shell silicon−carbon nanoparticles using the laser driven chemical vapor pyrolysis (LCVP). This continuous gas flow process enables the controlled synthesis of a large variety of nanoparticles and can be easily scaled-up to provide large quantities.[24] LCVP is based on the absorption of the infrared radiation emitted by a CO_2 laser by a flow of chemical precursors, leading to their thermal decomposition followed by nanoparticle nucleation and growth by collision assisted process. This very versatile process is particularly efficient for the production of silicon nanoparticles, often obtained in small agglomerates, and many studies report the control of both crystalline properties and size distribution.[24−30] Interestingly, this process is also efficient for the synthesis of carbon nanoparticles with controlled organization.[31,32]

On the basis of this background, we designed an original two-stage setup in order to synthesize silicon/carbon core−shell nanoparticles. Silicon cores are synthesized in the bottom stage and are immediately transferred by a carrier gas to the upper stage where the carbon shell is deposited on Si core in a second reaction zone. This new configuration is safer by design as no manipulation of nanomaterials is required between core and shell syntheses. It also ensures the protection of Si surface versus air oxidization. In this configuration, Si and Si@C nanoparticles with the same 30 nm silicon core size and the presence or not of a 2.5 nm carbon shell were synthesized in order to highlight the beneficial effect of the protective layer. The materials were characterized by both physical and electrochemical analyses using potentiodynamic sweep and galvanostatic cycling, thus demonstrating their interest as LIB anode active material.

RESULTS

Material synthesis by double stage laser pyrolysis. Si and Si@C nanoparticles were synthesized in a two-stage setup composed of two superposed reactors working under atmospheric pressure of Ar (Figure 1). In the first stage, the focalized laser beam interacts with a silane (SiH_4) flow resulting in the synthesis of silicon nanoparticles. The Ar carrier gas flow transfers them to the second stage where ethylene (C_2H_4) is inserted coaxially. The laser beam is transported by two mirrors to the second stage and defocalized in order to maximize the time of interaction between the C_2H_4 flow and the silicon cores. This second interaction results in the deposition of a carbon shell around the small agglomerates of silicon nanoparticles.

To compare Si and Si@C properties, we achieved two syntheses with or without addition of C_2H_4 flow at the second stage, all parameters being otherwise equal. The diameter of silicon nanoparticles was adjusted around 30 nm thanks to the dilution of SiH_4 with helium. Indeed, the high diffusion coefficient of helium in gases as well as its high thermal conductivity limits particle growth by collision/coagulation. Moreover, high gaseous flow rate accelerates the SiH_4 flow and decreases the time of residence of the growing Si seeds in the reaction zone.[26,33]

The laser power and focalization in the bottom stage was adjusted to favor a crystalline structure of the silicon cores, while keeping the remaining laser power in the second stage sufficient to ensure ethylene decomposition. Synthesis conditions in the first stage were chosen to maximize SiH_4 decomposition yield and avoid formation of silicon carbide in the second stage through unreacted SiH_4 and C_2H_4 mixture; 0.44 g of brown silicon nanoparticles and 0.68 g of dark gray Si@C nanoparticles were obtained in approximately 10 min of experiments for each material.

Physical Characterizations. Transmission electronic microscope images (TEM) of the Si and Si@C samples are reported in images a and b in Figure 2, whereas representative high-resolution TEM images (HRTEM) are displayed in images c and d in Figure 2. Figure 2e presents HRTEM image of a pure carbon nanoparticle present in the Si@C material and Figure 2f exposes a scanning transmission electronic microscope images (STEM) with electron energy loss spectroscopy (EELS) mapping analysis of one Si@C nanoparticle surface. In the case of silicon (Figure 2a), the sample consists in nanoparticles partially agglomerated with a chain-like morphology typical of gas phase synthesis, with narrow size distribution centered on 30 nm. HRTEM image (Figure 2c) shows a polycrystalline core with an amorphous shell of 3 nm attributed to SiO_x formation because of air

DOI: 10.1021/am5089742
ACS Appl. Mater. Interfaces 2015, 7, 6637−6644

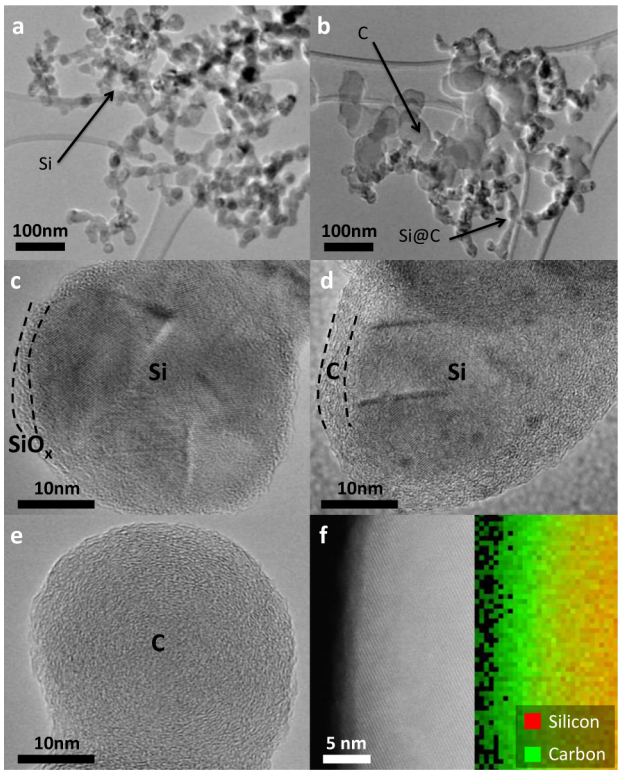

Figure 2. Bright-field TEM images of (a) Si and (b) Si@C nanoparticles. Relative bright-field HRTEM images of (c) one Si and (d) one Si@C nanoparticle highlighting SiO_x and C shell. (e) HRTEM image of one carbon nanoparticle from Si@C sample. (f) STEM-EELS mapping of silicon and carbon elements on the surface of one Si@C nanoparticle.

exposition, as expected for such particles.[34] Regarding the Si@C sample, TEM image (Figure 2b) highlights two populations with different sizes. The smallest size, around 30 nm, is attributed to Si@C nanoparticles while the larger size, around 50 nm, is attributed to nanoparticles composed of pure carbon. These latter particles may be formed by homogeneous nucleation in the excess C_2H_4 gas phase. The carbon coating of Si@C nanoparticles appears to encompass a whole silicon agglomerate. From Si@C HRTEM image (Figure 2d), the nanoparticles exhibit a polycrystalline silicon core size of 30 nm, similar to the Si sample, and a shell of approximately 2 to 2.5 nm thickness. One can note that no changes in average silicon core size neither than in chain-like structure have been detected between Si and Si@C nanoparticles. The HRTEM image from Figure 2**e** shows a pure carbon nanoparticle from Si@C sample mainly consisting of low organized sp^2 carbon with polyaromatic basic structural units, revealing an organization very similar to the one previously observed at low laser energy.[32] The carbon shell observed on Si@C sample also shows a similar structure. STEM and relative EELS mapping of silicon and carbon elements (Figure 2f) have been performed and confirm the carbon nature of the Si@C shell. An EELS spectrum of Si@C is displayed on Figure S4 (reported in Supporting Information), it brings more evidence to the low organized sp2 carbon nature of the shell.[35] More representative TEM, HRTEM and SEM images can be found in Supporting Information (Figure S5)

HRTEM images and STEM-EELS mapping cannot be considered as representative of the whole material, therefore Auger Electron Spectroscopy (AES) analysis of the samples have been performed to check the homogeneity of the carbon coating on a large scale. Figure 3 displays both AES spectra

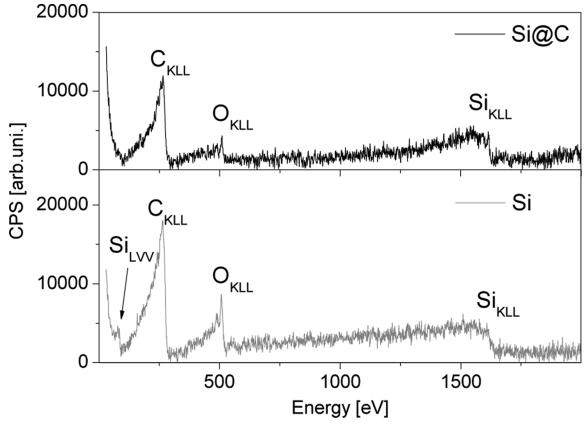

Figure 3. AES spectrum of Si and Si@C samples.

obtained on Si and Si@C samples, on a 100 nm side square area. Three particular transitions are of interest: the 1620 eV Si_{KLL}, the 80 eV Si_{LVV} and the 505 eV O_{KLL} transitions.

The C_{KLL} transitions cannot be used due to the carbon tape substrate used for these experiments. The Si_{KLL} transition remains with the same intensity in both spectra, whereas the O_{KLL} band is halved in Si@C compared to Si. Furthermore, the Si_{LVV} transition is almost absent in Si@C sample (reduced by a factor of 5). The escape depth of the electrons in carbon before losing 99% of the signal is about 12 nm at 1620 eV, but only 2.2 nm at 80 eV, by consequence the disappearance of the Si_{LVV} transition in the Si@C sample proves that the carbon shell is thicker than 2.2 nm on the surface of the whole analyzed domain.[36] Moreover, the decrease in the O_{KLL} transition intensity in Si@C compared to Si is bringing evidence to the protective role of the carbon layer against oxygen exposure.

XRD patterns and Raman spectra of Si and Si@C samples are presented in Figure 4a, b. On Figure 4a, all the peaks on both Si and Si@C samples can be ascribed to diamond cubic crystal structure of silicon. No silicon carbide phase is observed, this is encouraging for LIB application as this phase has a low ionic and electronic conductivity: its presence, particularly at the interface, would lower both the charge/discharge rate and the capacity of Si@C material. The average crystallite size for silicon, estimated using Sherrer's equation, is 10.3 nm for Si and 11.2 nm for Si@C.[37] Given the precision of this method, one can state that both samples present similar silicon crystallinity. As the crystallite size is lower than the effective core diameter (30 nm), this brings another evidence that the silicon cores are polycrystalline, in agreement with the HRTEM pictures. The diagram backgrounds measured for Si and Si@C samples show a significant difference: a bump below 25° confirms the presence of low organized sp^2 carbon in Si@C material. Raman spectroscopy presented in Figure 4b confirms this trend. In the bare Si spectra, the bands close to 500 and 960 cm^{-1} are typical of TO and 2TO crystalline silicon whereas the slight shoulder at 475 cm^{-1} is related to TO band of amorphous silicon. The weak contributions around 420 and 600 cm^{-1} are related to crystalline silicon LO and 2LA, TO+TA bands. The same Si related bands are present in the case of Si@C sample, with lower relative intensities because of the carbon coating and carbon nanoparticles dominating Raman signal. The two

DOI: 10.1021/am5089742
ACS Appl. Mater. Interfaces 2015, 7, 6637−6644

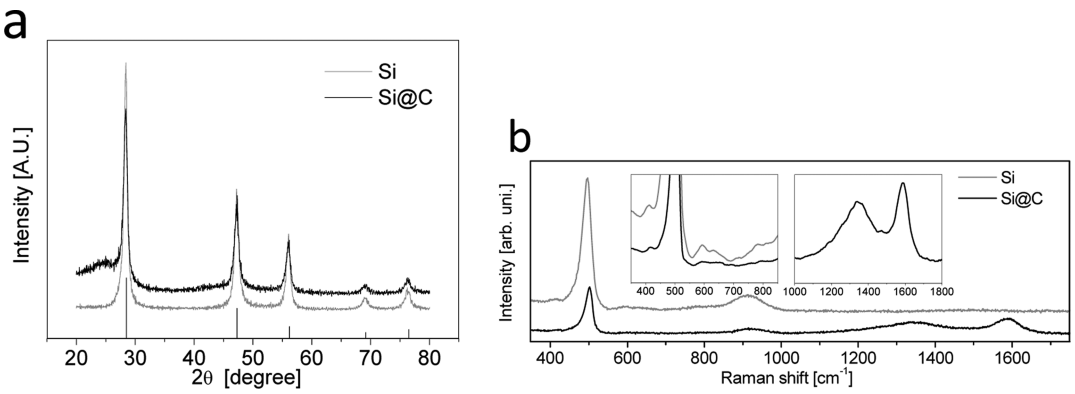

Figure 4. (a) Comparison of Si and Si@C XRD patterns and (b) Raman spectroscopy spectra.

features around 1360 and 1610 cm^{-1} are characteristic of a graphitic-like carbonaceous material. They can be deconvoluted into 5 contributions: the graphitic G bands (1580 cm^{-1}) and four disorder related contributions D1 (1350 cm^{-1}), D2 (1610 cm^{-1}), D3 (1500 cm^{-1}), and D4 (1250 cm^{-1}).[38] Deconvolution and fitting results are presented in the Supporting Information as Table S1 and Figure S3. G and D2 bands are assigned to lattice vibration of six-membered sp^2 rings into an ABAB stacking arrangement and at the surface of an ABAB stacking arrangement, respectively. D1 and D3 bands are identified as lattice vibration of six-membered sp^2 rings close to the edges of an ABAB stacking arrangement and without any stacking arrangement, respectively. These two bands can be related to the presence of short polyaromatic basic units. Finally, D4 band is related to the stretching of sp^2–sp^2, sp^3–sp^3, and sp^2–sp^3 carbon in noncyclic configuration. The presence of the D4 band, as the intensity ratio I_{D1}/I_G of 1.02, confirm that the carbon shell is poorly organized, as expected by the XRD analysis and the HRTEM images.[39]

Thermogravimetric analyses performed on the two powders are showed in Figure 5. These curves reveal a similar oxidation

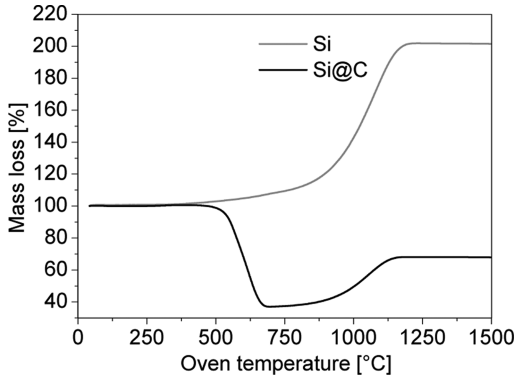

Figure 5. Normalized thermogravimetric signals of Si and Si@C nanoparticles between 40 and 1500 °C with heating rate of 10 °C min^{-1}.

of silicon between 750 and 1200 °C for both Si and Si@C samples, whereas oxidation of carbon is observed between 400 and 700 °C for Si@C sample only and corresponds to a large weight loss. From this loss, the C amount in Si@C material can be estimated at 62%wt. A measurement of carbon content using a chemical analyzer (63.5 wt %) confirmed this result. It indicates the presence of many carbon nanoparticles in addition to the carbon coated silicon nanoparticles. Indeed, considering 30 nm silicon spheres with a 2 to 2.5 nm shell, the carbon mass is approximately distributed 20 wt % in the carbon shells and 80%wt in carbon nanoparticles.

Carbon texture in both shell and free nanoparticles strongly influence the Brunauer–Emmett–Teller (BET) specific surface area as bare silicon develops 66 $m^2\ g^{-1}$, whereas Si@C material develops 156 $m^2\ g^{-1}$. The huge specific surface area measured in the latter case is correlated to the high porosity encountered in disordered carbon structures.

In summary, two samples with similar Si polycrystalline core of 30 nm diameter were obtained, one being covered by an approximately 2 to 2.5 nm low organized sp^2 carbon shell. Interestingly, Stournara et al. have demonstrated, using ab initio calculations, that the carbon layer around round-shaped silicon nanoparticles must be low organized and close to 2.5 nm thickness in order to minimize the debonding or fracture effects.[40] We study in the next section the beneficial effect of this shell on the electrochemical properties.

■ ELECTROCHEMICAL EXPERIMENTS

Si and Si@C materials were tested as anode material in coin–cell configuration versus metallic lithium between 1 V and 5 mV with two distinct modes: potentiodynamic and galvanostatic. Galvanostatic mode gives information on capacity and cyclability, while potentiodynamic experiments highlight degradation effects on the lithiation and delithiation properties. The capacity of the low organized sp^2 carbon is approximately 100 mAh g^{-1} (see Figure S1 and S2 in the Supporting Information). Therefore, the active masses have been considered as the amount of silicon and carbon shells, i.e., without taking into account the mass of the carbon nanoparticles present in the Si@C sample neither the mass of the carbon additives. A theoretical specific capacity of 3579 mAh g^{-1} was considered for silicon.

Potentiodynamic Sweeps. Figure 6a–c shows cyclic voltammetry of Si and Si@C anodes. Figure 6a shows the typical first lithiation sweep of pristine Si and Si@C anodes operating from open circuit voltage (OCV) to 5 mV vs Li^+/Li at 20 $\mu V.s^{-1}$. During the first lithiation of both materials, 5 anodic reactions occurred. Two broad peaks at 1.8 and 1.4 V are attributed to the polymerization of fluoroethylene carbonate (FEC). In the case of Si anode, the sharp peak located at 1.2 V is related to vinylene carbonate (VC) polymerization, lowered to 0.9 V in the case of Si@C anode. The 0.3 V shift can be attributed to the chemical difference between the two surfaces: VC decomposition is much more efficient on oxygen rich SiO_x surface of Si nanoparticles than on the carbon surface of Si@C material, lowering the reduction potential in this latter case.[41] The small peak at 0.5 V on the bare Si anode sweep corresponds to the formation of SEI from ethyl carbonate/diethyl carbonate (EC/DEC) decomposition.[42,43] This peak is shifted to 0.6 for Si@C anode and is much wider, indicating a difference in the SEI formation, probably due to the larger specific surface area. Finally, a strong anodic current near

DOI: 10.1021/am5089742
ACS Appl. Mater. Interfaces 2015, 7, 6637–6644

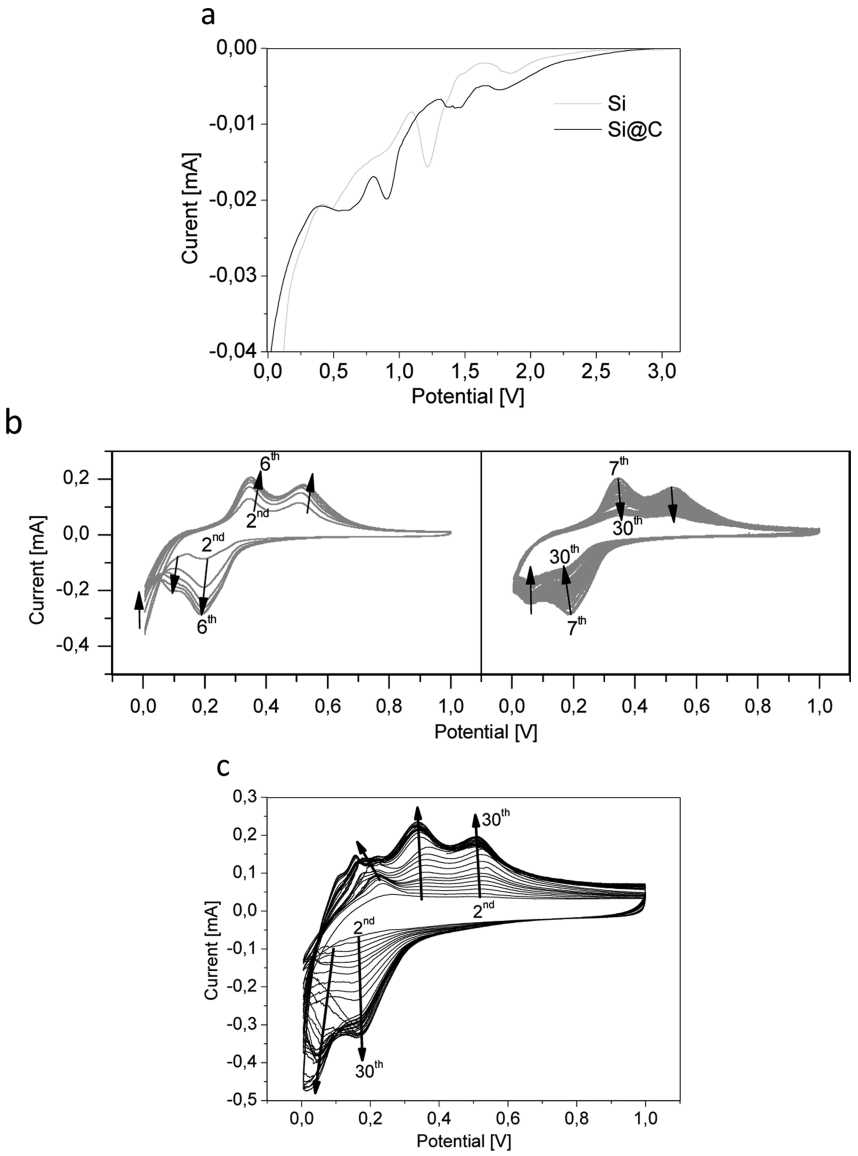

Figure 6. (a) First lithiation of pristine Si and Si@C anode between OCV and 5 mV at 20 μV s^{-1}, 30 following cycles of (b) Si and (c) Si@C. The arrows indicate the evolution of signals.

5 mV is attributed to single phase transition from crystalline Si to an highly lithiated amorphous phase close to $Li_{3.1}Si$.[44]

Figure 6b, c shows the 30 following sweeps between 1 V and 5 mV of Si and Si@C anode. For clarity, in the case of Si sample, we separated the 5 first sweeps (on the left panel) from the rest of the voltammetry (on the right panel). Two anodic peaks are observed around 0.19 and 0.10 V and two cathodic peaks at 0.35 and 0.52 V. On the left panel, the intensities increase from the second cycle to the sixth cycle and are related to the classical signature of silicon lithiation and delithiation without $Li_{3.75}Si$ crystallization.[45] At the same time, the anodic wave near 5 mV progressively decreases, in relation with the amorphization of c-Si. Although the silicon is progressively amorphised, more and more material is lithiated, resulting in the increase of all the signals. One can note that no crystallization of the $Li_{3.75}Si$ phase is observed as no such related delithiation signal is detected: Si materials do not spend enough time at 5 mV for this crystallization to occur. On the left panel, the previous tendency is reversed, and all the signals decrease, meaning that less and less active material takes part in the lithiation. Even at the nanometric scale, the large volume changes have a huge impact on SEI stability. As a consequence, electrode porosity is progressively filled up by the electrolyte decomposition products, and less and less active material is connected to ionic and electronic networks.[8]

Figure 6c presents the same experiment conducted on Si@C material. The same anodic and cathodic silicon related processes are present, plus a new set of delithiation peaks from carbon in the 0.1 to 0.2 V area. However, the evolution of the signal upon the sweep is noticeably different from the bare Si nanoparticles based anode. From the second to the 12th cycles, all the signals are growing in intensity and finally stabilize to a maximum position for the remaining sweeps indicating that no severe degradation mechanism happens. The Si@C material needs more cycles to be completely amorphised (11 instead of 5 for Si sample), in agreement with a low resistive contribution of the carbon shell. Nevertheless, this behavior suggests that the shell efficiently limits the silicon core to direct exposure of the electrolyte. One can note the evolution of the carbon delithiation peaks, starting from one wide bump and resulting at the end of the 30th cycle in 3 sharper peaks at 0.10, 0.15, and 0.22 V. This can be explained by the progressive lithiation of carbon nanoparticles. Regarding of this hypothesis, we have studied the behavior of these carbon species and shown that they bring very small capacity into the Si@C nanomaterial and therefore can be neglected (for more details, refer to the Supporting Information).

DOI: 10.1021/am5089742
ACS Appl. Mater. Interfaces 2015, 7, 6637−6644

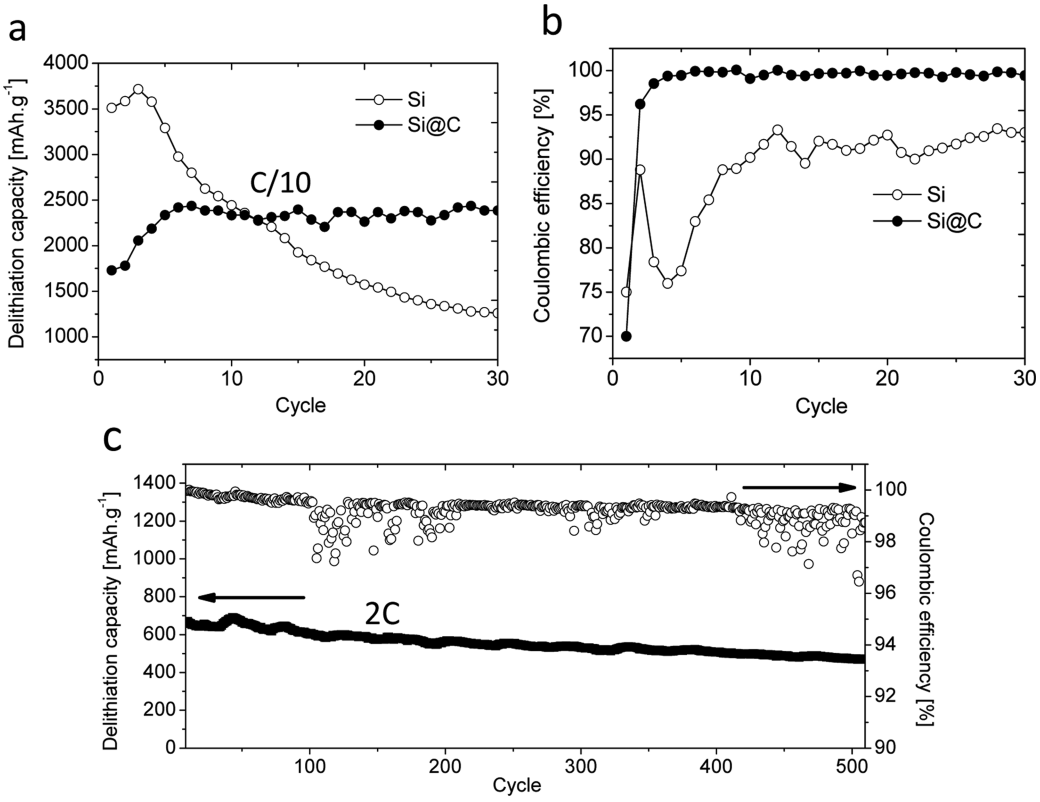

Figure 7. (a) Delithiation capacity at *C*/10 rate of Si and Si@C and (b) relative Coulombic efficiency. (c) Delithiation capacity at 2*C* rate and relative Coulombic efficiency of Si@C.

These experiments clarified various mechanisms occurring in both materials. Protecting the silicon with a carbon shell improves the stability of the whole electrode, solving the SEI stability issue. At the opposite, the electrode made from bare Si core is very unstable through lithiation/delithiation process. However, potentiodynamic method is not fully representative of the real cycling behavior of silicon. Indeed, kinetic behavior is very different and the materials undergo very long time under 0.1 V, which is a critical zone for solvents decomposition. It may virtually decrease the stability properties of bare Si material. To confirm the improved stability of anode made from Si@C material, we conducted galvanostatic cycling tests.

Galvanostatic Cycling. Cyclability of Si and Si@C materials in coin-cell configuration versus metallic lithium was studied. Figure 7a displays Si and Si@C delithiation capacities while Figure 7b reports their respective Coulombic efficiency.

Pure silicon exhibits a very high capacity during the first cycles with very poor cycling stability. The reversible capacity decreases over 30 cycles from 3250 to 1200 mAh g^{-1} together with a low Coulombic efficiency. This behavior is not surprising, Tarascon et al. mentioned a similar result when using nanosized crystalline silicon synthesized from laser pyrolysis of silane.[14] On the other hand, Si@C material shows a high capacity of 2300 mAh.g[1] and a good Coulombic efficiency of 99.6%. The first irreversible loss is greater with Si@C sample than with Si sample, probably due to the larger specific surface area of Si@C nanoparticles. First lithiation and delithiation curves of Si and Si@C can be found in the Supporting Information (Figure S6 and S7). Surprisingly, the full reversible theoretical capacity of Si in Si@C sample is not reached. Xiao X. et al. proved that thick graphitic carbon layer (20 nm) can effectively stop the volume expansion of silicon core due to compressive stress induced by carbon shell, raising the activation energy for diffusion of Li in Si, thus limiting the capacity. However, such behavior is not likely to happen in the case of 2.5 nm thick carbon shell.[46] Figure 7c shows high cyclability of Si@C material at the high rate of 2*C* with a slight decrease of capacity from 700 to 500 mAh g^{-1} after 500 cycles. The Coulombic efficiency is superior to 99.7% during the first cycles, then around 99.6, 99.3, and 99.2% at respectively 100, 300, and 500 cycles. These galvanostatic results confirm the enhanced cycling stability and capacity of Si@C material. The amorphous structure of the carbon shells allows accommodation of the volumetric change of silicon without breaking, thus preventing the formation of extra SEI responsible for active material loss and capacity fading. The presence of rich sp^2 carbon nanoparticles could be highly reduced by further improvement of the LCVP setup, in particular by tuning the method of ethylene injection and favoring nucleation process. However, as a perspective, it can be considered to elaborate new electrode using the material composed of Si@C + carbon nanoparticles after an adequate thermic treatment to induce enhanced electronic conductivity. Doing so, no electronic percolator should be added to the formulation as carbon nanoparticles are in close contact to the active material.

CONCLUSION

For the first time, we showed that an original configuration of LCVP allows synthetizing silicon nanoparticles covered by a continuous carbon shell in a one step process. STEM-EELS analysis confirmed the carbonaceous nature of the shell while AES proved that the whole Si@C material is covered with carbon and that the silicon surface is less oxidized compared to Si nanoparticles. Compared to bare Si nanoparticles produced in the same reactor, the impact of the carbon shell on cyclability and electrochemical performances is significant as both the cyclability and the Coulombic efficiency are greatly enhanced. The potentiodynamic experiences highlight the excellent stability of Si@C material after few stabilization cycles. This performance can be attributed to the protective effect of the carbon layer, limiting direct contact between the electrolyte and the silicon surface. As a result of this high stability, Si@C

DOI: 10.1021/am5089742
ACS Appl. Mater. Interfaces 2015, 7, 6637−6644

material can be cycled over 500 cycles with a capacity up to 500 mAh g^{-1} at the high charge/discharge rate of 2*C*.

METHODS

Material Synthesis. Nanosized silicon and carbon covered silicon nanoparticles were synthesized by an original two stages LCVP setup. Trumpf TLF 2400 CO_2 laser operating at 18 kHz was used for the decomposition of silane (Messer UHP grade, 99.99%) and ethylene (Alfa Gaz UHP grade).

In the lower reaction zone, the size of Si nanoparticles was tuned by both He (Messer 4.5 grade) dilution and focalization of the laser beam using a 500 mm cylindrical ZnSe lens (Wavelength-Tech, Ronar-Smith) while the pressure was regulated at 740 Torr. The silicon nanopowders were transferred by a laminar Argon flow (Messer 6.0 grade) to the upper reaction zone where they are covered with carbon. The powders are collected downstream on porous filters.

Material Characterization. The powders are characterized using a Phillips CM12 TEM operating at 80 kV and Phillips CM200 HRTEM operating at 150 kV. The samples were prepared by suspending the powders into ethanol and then deposited onto Agar Scientific lacey carbon-coated grids. STEM-EELS experiments were conducted using a FEI Titan Ultimate microscope equipped with a monochromator and double spherical aberration correctors (Cs) for both the probe-forming and the image-forming lenses. The microscope was operating at an accelerating voltage of 200 kV using a 20 mrad convergence semiangle. STEM images were collected using a high-angle annular dark field detector, where inner and outer semiangles were 60 and 180 mrad, respectively. EELS map was acquired using a Gatan GIF Quantum in the Dual EELS mode allowing the simultaneous collection of the low loss and core loss spectra. Acquisition times were 1 μs and 20 ms respectively and the collection semiangle was 35 mrad. TGA measurements were conducted using a Setaram 92−16,18. A temperature ramp from 20 to 1500 °C and a heat speed of 10 °C min^{-1} were set. Results from TGA were confirmed using a Horiba EMIA-V2 carbon−sulfur analyzer.

BET surfaces measurements were performed using a Micromeritics Automat 23. XRD diagrams were obtained using a Siemens D5000 diffractometer. Raman spectra were recorded using a Renishaw InVia Raman Microscope with a 532 nm laser line. AES was achieved using a PHI 700Xi scanning nanoprobe from Physical Electronics. The powders were deposited on Agar Scientific double sided carbon adhesive discs. Chamber pressure was set to 5×10^{-9} Torr and samples were analyzed with an accelerating voltage of 20 kV and 1 nA intensity. The square areas analyzed are approximately 100 nm sided.

Electrode Preparation. Super P was purchased from Timcal and vapor grown carbon fibers (VGCF) were purchased from ShowaDenko. They were used as electronic percolators at small and long-range without further purification. Carboxymethylcellulose (DS = 0.7, M_w = 250 kg mol^{-1}) was purchased from Sigma-Aldrich and diluted in pure distillated water. Slurry of the active material was prepared with a (50/12.5/12.5/25) formulation of (active material/C65/VGCF/CMC). Mass loading of the slurry was adjusted in order to provide homogeneous slurry with good dispersion of all components. Using a doctor blade coating machine, a uniform 100 μm layer was deposited on a 10 μm Cu foil. After drying, the mass loading of the active material is approximately 0.59 mg cm^{-2} ± 8% for the Si@C and 0.57 mg cm^{-2} ± 2% for the Si. Ø14 mm pellets were obtained from the electrode sheets and then pressed under 1 T. CR2032 half-cell batteries were assembled in Ar-filled glovebox with both Si and Si@C materials. Viledon paper was soaked in $LiPF_6$-EC:DEC (1M-1;1) electrolyte containing 2 wt % vinylcarbonate and 10 wt % fluoroethylene carbonate. Celgard was used as separator. Li metal discs (2.01 cm^2) were used as counter electrode.

Electrochemical Testing. Cyclic voltammetry experiments were performed by a VMP-3 system (Biologic) in the range of 5 mV to 1 V vs Li^+/Li at 20 μV s^{-1}. Electrochemical cycling was performed by galvanostatic charge/discharge of the coin-cells in the range of 5 mV to 1 V vs Li^+/Li, monitored by an ARBIN bench system.

ASSOCIATED CONTENT

Supporting Information

Cyclic voltammetry and galvanostatic cycling of carbon species, Si@C Raman spectra deconvolution, EELS spectra, additional TEM, HRTEM, and SEM images, and first charge/discharge curves. This material is available free of charge via the Internet at http://pubs.acs.org.

AUTHOR INFORMATION

Corresponding Authors

*E-mail: julien.sourice@cea.fr (J.S.).
*E-mail: nathalie.herlin@cea.fr (N.H.-B.).

Author Contributions

The manuscript was written through contributions of all authors. All authors have given approval to the final version of the manuscript.

Funding

This work was supported by grants from CEA LITEN

Notes

The authors declare no competing financial interest.

ACKNOWLEDGMENTS

This research was supported by LITEN/DEHT (CEA Grenoble). The authors are very thankful to Jean-Noël Rouzaud (ENS Paris) for his contribution in HRTEM microscopy, Henri Perez (LEDNA) for electrochemical testing, Servane Coste (INSTN) for X-ray diffraction, Mickael Bouhier (LAPA) for Raman Spectroscopy, and Aurélie Habert for BET analysis (LEDNA).

REFERENCES

(1) Scrosati, B.; Garche, J. Lithium Batteries: Status, Prospects and Future. *J. Power Sources* **2010**, *195*, 2419−2430.
(2) Su, X.; Wu, Q.; Li, J.; Xiao, X.; Lott, A. Silicon Based Nanomaterials for Lithium Ion Batteries: A Review. *Adv. Energy Mater.* **2014**, 1−23.
(3) Park, M.-H.; Kim, M. G.; Joo, J.; Kim, K.; Kim, J.; Ahn, S.; Cui, Y.; Cho, J. Silicon Nanotube Battery Anodes. *Nano Lett.* **2009**, *9*, 3844−3847.
(4) Kasavajjula, U.; Wang, C.; Appleby, a. J. Nano- and Bulk-Silicon-Based Insertion Anodes for Lithium-Ion Secondary Cells. *J. Power Sources* **2007**, *163*, 1003−1039.
(5) Kim, T.-H.; Park, J.-S.; Chang, S. K.; Choi, S.; Ryu, J. H.; Song, H.-K. The Current Move of Lithium Ion Batteries Towards the Next Phase. *Adv. Energy Mater.* **2012**, *2*, 860−872.
(6) Wu, H.; Cui, Y. Designing Nanostructured Si Anodes for High Energy. *Nano Today* **2012**, *7*, 414−429.
(7) Scrosati, B.; Hassoun, J.; Sun, Y.-K. Lithium-Ion Batteries. A Look into the Future. *Energy Environ. Sci.* **2011**, *4*, 3287−3295.
(8) Radvanyi, E.; Porcher, W.; De Vito, E.; Montani, A.; Franger, S.; Jouanneau Si Larbi, S. Failure Mechanisms of Nano-Silicon Anodes upon Cycling: An Electrode Porosity Evolution Model. *Phys. Chem. Chem. Phys.* **2014**, *16*, 17142−17153.
(9) Profatilova, I. a.; Stock, C.; Schmitz, A.; Passerini, S.; Winter, M. Enhanced Thermal Stability of a Lithiated Nano-Silicon Electrode by Fluoroethylene Carbonate and Vinylene Carbonate. *J. Power Sources* **2013**, *222*, 140−149.
(10) Mazouzi, D.; Lestriez, B.; Roué, L.; Guyomard, D. Silicon Composite Electrode with High Capacity and Long Cycle Life. *Electrochem. Solid-State Lett.* **2009**, *12*, 215−218.
(11) Zhou, M.; Cai, T.; Pu, F.; Chen, H.; Wang, Z.; Zhang, H.; Guan, S. Graphene/carbon-Coated Si Nanoparticle Hybrids as High-Performance Anode Materials for Li-Ion Batteries. *ACS Appl. Mater. Interfaces* **2013**, *5*, 3449−3455.

DOI: 10.1021/am5089742
ACS Appl. Mater. Interfaces 2015, 7, 6637−6644

(12) Erk, C.; Brezesinski, T.; Sommer, H.; Schneider, R.; Janek, J. Toward Silicon Anodes for next-Generation Lithium Ion Batteries: A Comparative Performance Study of Various Polymer Binders and Silicon Nanopowders. *ACS Appl. Mater. Interfaces* **2013**, *5*, 7299−7307.
(13) Wu, H.; Chan, G.; Choi, J. W.; Ryu, I.; Yao, Y.; McDowell, M. T.; Lee, S. W.; Jackson, A.; Yang, Y.; Hu, L.; Cui, Y. Stable Cycling of Double-Walled Silicon Nanotube Battery Anodes through Solid-Electrolyte Interphase Control. *Nat. Nanotechnol.* **2012**, *7*, 310−315.
(14) Saint, J.; Morcrette, M.; Larcher, D.; Laffont, L.; Beattie, S.; Pérès, J.-P.; Talaga, D.; Couzi, M.; Tarascon, J.-M. Towards a Fundamental Understanding of the Improved Electrochemical Performance of Silicon−Carbon Composites. *Adv. Funct. Mater.* **2007**, *17*, 1765−1774.
(15) Lee, K. J.; Yu, S.-H.; Kim, J.-J.; Lee, D.-H.; Park, J.; Seo, S.-S.; Cho, J. S.; Sung, Y.-E. $Si_7Ti_4Ni_4$ as a Buffer Material for Si and Its Electrochemical Study for Lithium Ion Batteries. *J. Power Sources* **2013**, *246*, 729−735.
(16) Qu, J.; Li, H.; Henry, J. J.; Martha, S. K.; Dudney, N. J.; Xu, H.; Chi, M.; Lance, M. J.; Mahurin, S. M.; Besmann, T. M.; Dai, S. Self-Aligned Cu−Si Core−shell Nanowire Array as a High-Performance Anode for Li-Ion Batteries. *J. Power Sources* **2012**, *198*, 312−317.
(17) Zhang, T.; Gao, J.; Zhang, H. P.; Yang, L. C.; Wu, Y. P.; Wu, H. Q. Preparation and Electrochemical Properties of Core−Shell Si/SiO Nanocomposite as Anode Material for Lithium Ion Batteries. *Electrochem. Commun.* **2007**, *9*, 886−890.
(18) Terranova, M. L.; Orlanducci, S.; Tamburri, E.; Guglielmotti, V.; Rossi, M. Si/C Hybrid Nanostructures for Li-Ion Anodes: An Overview. *J. Power Sources* **2014**, *246*, 167−177.
(19) Cui, L.; Yang, Y.; Hsu, C.; Cui, Y. Carbon− Silicon Core− Shell Nanowires as High Capacity Electrode for Lithium Ion Batteries. *Nano Lett.* **2009**, *9*, 1−5.
(20) Xu, Y.; Yin, G.; Ma, Y.; Zuo, P.; Cheng, X. Nanosized Core/shell Silicon@carbon Anode Material for Lithium Ion Batteries with Polyvinylidene Fluoride as Carbon Source. *J. Mater. Chem.* **2010**, *20*, 3216−3220.
(21) Bang, B. M.; Kim, H.; Song, H.-K.; Cho, J.; Park, S. Scalable Approach to Multi-Dimensional Bulk Si Anodes via Metal-Assisted Chemical Etching. *Energy Environ. Sci.* **2011**, *4*, 5013−5019.
(22) Yi, R.; Dai, F.; Gordin, M. L.; Sohn, H.; Wang, D. Influence of Silicon Nanoscale Building Blocks Size and Carbon Coating on the Performance of Micro-Sized Si-C Composite Li-Ion Anodes. *Adv. Energy Mater.* **2013**, *3*, 1507−1515.
(23) Chaukulkar, R. P.; de Peuter, K.; Stradins, P.; Pylypenko, S.; Bell, J. P.; Yang, Y.; Agarwal, S. Single-Step Plasma Synthesis of Carbon-Coated Silicon Nanoparticles. *ACS Appl. Mater. Interfaces* **2014**.
(24) Swihart, M. Vapor-Phase Synthesis of Nanoparticles. *Curr. Opin. Colloid Interface Sci.* **2003**, *8*, 127−133.
(25) Huisken, F.; Ledoux, G.; Guillois, O.; Reynaud, C. Light-Emitting Silicon Nanocrystals from Laser Pyrolysis. *Adv. Mater.* **2002**, *14*, 1861−1865.
(26) Sublemontier, O.; Kintz, H.; Lacour, F. Synthesis and on-Line Size Control of Silicon Quantum Dots. *KONA Powder Part. J.* **2011**, *29*, 236−250.
(27) Sublemontier, O.; Lacour, F.; Leconte, Y.; Herlin-Boime, N.; Reynaud, C. CO2 Laser-Driven Pyrolysis Synthesis of Silicon Nanocrystals and Applications. *J. Alloys Compd.* **2009**, *483*, 499−502.
(28) Trave, E.; Bello, V.; Mattei, G.; Mattiazzi, M.; Borsella, E.; Carpanese, M.; Fabbri, F.; Falconieri, M.; D'Amato, R.; Herlin-Boime, N. Surface Control of Optical Properties in Silicon Nanocrystals Produced by Laser Pyrolysis. *Appl. Surf. Sci.* **2006**, *252*, 4467−4471.
(29) Cauchetier, M.; Croix, O.; Luce, M.; Michon, M. Laser Synthesis of Ultrafine Powders. *Ceram. Int.* **1987**, *13*, 13−17.
(30) Cannon, W.; Danforth, S. Sinterable Ceramic Powders from Laser-Driven Reactions: II, Powder Characteristics and Process Variables. *J. Am. Ceram. Soc.* **1982**, 330−335.
(31) Alexandrescu, R.; Crunteanu, A. Synthesis of Carbon Nanotubes by CO 2-Laser-Assisted Chemical Vapour Deposition. *Infrared Phys. Technol.* **2003**, *44*, 43−50.
(32) Galvez, A.; Herlin-Boime, N.; Reynaud, C. Carbon Nanoparticles from Laser Pyrolysis. *Carbon* **2002**, *40*, 2775−2789.
(33) Lacour, F.; Guillois, O.; Portier, X.; Perez, H.; Herlin, N.; Reynaud, C. Laser Pyrolysis Synthesis and Characterization of Luminescent Silicon Nanocrystals. *Phys. E* **2007**, *38*, 11−15.
(34) Huisken, F.; Hofmeister, H.; Kohn, B.; Laguna, M. .; Paillard, V. Laser Production and Deposition of Light-Emitting Silicon Nanoparticles. *Appl. Surf. Sci.* **2000**, *154−155*, 305−313.
(35) Garvie, L. A. J.; Crave, A. J. Fine Structure in the Study of Minerals Use of Electron-Energy Arsrucr. *Am. Mineral.* **1994**, *79*, 411−425.
(36) Tanuma, S.; Powell, C. J. Electron Inelastic Mean Free Paths. *Surf. Interface Anal.* **1993**, *21*, 165−176.
(37) Patterson, A. L. The Scherrer Formula for X-Ray Particle Size Determination. *Phys. Rev.* **1939**, *56*, 978−982.
(38) Santamaria, A.; Falco, G.; De Commodo, M. Raman Features Between Two Clases of Carbon Nanoparticles Generated in Ethylene Flames. Meet. Ital. *Sect. Combust. Inst.* **2013**, 2−7.
(39) Pimenta, M. a; Dresselhaus, G.; Dresselhaus, M. S.; Cançado, L. G.; Jorio, A.; Saito, R. Studying Disorder in Graphite-Based Systems by Raman Spectroscopy. *Phys. Chem. Chem. Phys.* **2007**, *9*, 1276−1291.
(40) Stournara, M. E.; Qi, Y.; Shenoy, V. B. From Ab Initio Calculations to Multiscale Design of Si/C Core-Shell Particles for Li-Ion Anodes. *Nano Lett.* **2014**, *14*, 2140−2149.
(41) Ota, H.; Sakata, Y.; Inoue, A.; Yamaguchi, S. Analysis of Vinylene Carbonate Derived SEI Layers on Graphite Anode. *J. Electrochem. Soc.* **2004**, *151*, 1659−1669.
(42) Chen, L.; Wang, K.; Xie, X.; Xie, J. Effect of Vinylene Carbonate (VC) as Electrolyte Additive on Electrochemical Performance of Si Film Anode for Lithium Ion Batteries. *J. Power Sources* **2007**, *174*, 538−543.
(43) Kim, J. S.; Byun, D.; Lee, J. K. Electrochemical Characteristics of Amorphous Silicon Thin Film Electrode with Fluoroethylene Carbonate Additive. *Curr. Appl. Phys.* **2014**, *14*, 596−602.
(44) Radvanyi, E.; De Vito, E.; Porcher, W.; Danet, J.; Desbois, P.; Colin, J.-F.; Si Larbi, S. J. Study of Lithiation Mechanisms in Silicon Electrodes by Auger Electron Spectroscopy. *J. Mater. Chem. A* **2013**, *1*, 4956−4965.
(45) Zamfir, M. R.; Nguyen, H. T.; Moyen, E.; Lee, Y. H.; Pribat, D. Silicon Nanowires for Li-Based Battery Anodes: A Review. *J. Mater. Chem. A* **2013**, *1*, 9566.
(46) Xiao, X.; Zhou, W.; Kim, Y.; Ryu, I.; Gu, M.; Wang, C.; Liu, G.; Liu, Z.; Gao, H. Regulated Breathing Effect of Silicon Negative Electrode for Dramatically Enhanced Performance of Li-Ion Battery. *Adv. Funct. Mater.* **2015**, n/a−n/a.

DOI: 10.1021/am5089742
ACS Appl. Mater. Interfaces 2015, 7, 6637−6644